Acta Biomaterialia 226 (2026) 770–780

Contents lists available at ScienceDirect

Acta Biomaterialia

journal homepage: www.elsevier.com/locate/actbio

Full length article

Atom probe tomography shows defect-driven degradation in plasma electrolytic oxidation-coated Mg-Ca alloys

Selase Torkornoo [a,*], Eric Woods [b], Yongqiang Kang [a], Raymond Kwesi Nutor [a], Qiuying Ji [a], Leopold Berger [c], Thomas Imwinkelried [d], Baptiste Gault [a,e,*]

[a] Department of Circular Metallurgy and Alloy Design, Max-Planck-Institut für Nachhaltige Materialien GmbH, Düsseldorf, Germany
[b] Lehrstuhl für Mikro- und Nano-Analytik, INCYTE, Universität Siegen, Siegen, Germany
[c] Kairos Medical AG, Bettlach, Switzerland
[d] RMS Foundation, Bettlach, Switzerland
[e] Groupe de Physique des Matériaux, Université de Rouen Normandie, Rouen, France

ARTICLE INFO

Keywords:
Magnesium alloys
Mg–Ca
Plasma electrolytic oxidation
Atom probe tomography

ABSTRACT

Magnesium alloys are promising biodegradable implant materials, but often suffer from rapid corrosion and uncontrolled hydrogen evolution in physiological environments, calling for robust surface modification strategies to regulate degradation and gas release. Plasma electrolytic oxidation (PEO) coatings are produced on an ultra-high-purity Mg-0.45 wt. % Ca alloy using two phosphate-based electrolytes and characterized by advanced electron microscopy and atom probe tomography (APT) to resolve their multi-layered structure, phase composition, and nanoscale defects. Both coatings form a tri-layered structure: a dense crystalline MgO layer, a porous inner MgO/amorphous phosphorus-rich layer, and an outer amorphous phosphorus-rich layer modulated by electrolyte ions. APT reveals nanoscale pores, Na segregation, and H-enriched surface products after corrosion. Early-stage *in vitro* testing in Hank's solution shows uniform dissolution of the dense outer layer of the coating formed in the ammonia-based electrolyte, accompanied by cracking and delamination in the inner layer. This links the observed defects to the degradation pathways and enhanced susceptibility to localized attack within the coating. These insights reveal how electrolyte chemistry controls phase balance, porosity, and corrosion resistance, guiding the design of PEO coatings for enhanced implant longevity.

Statement of significance: Understanding and controlling the degradation of Mg-based biomaterials remains a central challenge for their clinical adoption. This study establishes a nanoscale mechanistic framework linking the chemistry of plasma electrolytic oxidation (PEO) coatings to the corrosion behavior of a Mg–Ca alloy in Hank's balanced salt solution (HBSS). By combining atom probe tomography (APT) with advanced microscopy analyses, we reveal that Na accumulation within defects and the amorphous coating regions are key drivers of localized corrosion and coating instability. These insights redefine the current understanding of PEO coating performance and establish new principles for desigining degradation-resistant, clinically viable, biodegradable implants.

1. Introduction

Biodegradable implants made of magnesium (Mg) have garnered substantial attention for their biocompatibility, role in important biological functions, and low density [1]. In addition, Mg has both a Young's modulus and a compressive yield strength comparable to bone [2]. Mg also plays a role in nearly 300 enzymatic functions, including indispensable reactions in adenosine triphosphate metabolism, which is essential to life [3,4]. A factor limiting the deployment of Mg implants is their low corrosion resistance, which can be adjusted through purification and alloying. However, the alloying elements promote the formation of a multi-phase microstructure, creating potential differences between phases that drive micro-galvanic corrosion and compromise the integrity of the Mg surface [5].

Calcium (Ca) is a physiologically compatible alloying element for novel Mg alloys designed for use as bone implants, since it is the most abundant component of healthy bone composition. Mg-Ca alloys are typically composed of two phases, α-Mg and Mg_2Ca, with mechanical

* Corresponding authors at: Department of Circular Metallurgy and Alloy Design, Max-Planck-Institut für Nachhaltige Materialien GmbH, Düsseldorf, Germany.
E-mail addresses: s.torkornoo@mpi-susmat.de (S. Torkornoo), baptiste.gault1@univ-rouen.fr (B. Gault).

https://doi.org/10.1016/j.actbio.2026.10.022
Received 7 May 2026; Accepted 13 October 2026
Available online 14 October 2026
1742-7061/© 2026 The Authors. Published by Elsevier Inc. on behalf of Acta Materialia Inc. This is an open access article under the CC BY license (http://creativecommons.org/licenses/by/4.0/).
Open access funding enabled and organized by Projekt DEAL.

properties adjustable by Ca content (x = 0.2 – 3 wt. %) [6–9]. Meanwhile, the corrosion rate of Mg-Ca alloy increases monotonically with increasing Ca concentration up to the solubility limit of Ca in Mg of 1.34 wt. % Ca [10]. As the alloy degrades, the release of Ca^{2+} and Mg^{2+} ions from Mg–Ca alloys can enhance osteoblast adhesion, proliferation, and differentiation, thereby promoting bone regeneration [11,12].

Mg degradation behavior is accompanied by hydrogen (H_2) gas evolution, and the presence of H_2 gas in proximity to Mg implants has been observed to induce both inflammatory and mechanical responses in peri-implant tissue and cells, including changes in cell morphology and tissue strain [13]. In contrast, H_2 has shown therapeutic efficacy in oxidative stress, apoptosis, energy metabolism regulation, immune modulation, and the regulation and modulation of inflammation [14,15]. This underscores the importance of regulating the release of H_2 gas from Mg implants.

One approach for delaying H_2 generation and enhancing bioactivity is surface modifications, and among the different coating techniques, plasma electrolytic oxidation (PEO) or microarc oxidation stands out. PEO is a high-voltage plasma-assisted oxidation process that promotes the dissolution of a pre-existing oxide film, the formation of an anodic barrier film, and a porous oxide layer [16]. The thickness, porosity, and morphology of the oxide layer formed by PEO are strongly influenced by a number of process parameters and conditions, including the electrolyte, applied voltage/current density, frequency, duty cycle, and treatment time [16]. The growth of the coating thickness is positively correlated with increasing applied voltage [17,18] and treatment time [19,20], while morphological features such as pore and phase formation are enhanced by a change in conductivity and composition of electrolytes [21]. Importantly, recent *in vivo* studies have shown that PEO-coated Mg alloys can improve degradation rates by decreasing H_2 gas release [22], and enhanced osseointegration (24.62% ± 13.48% new bone) compared to uncoated ones (10.20% ± 8.80%) [23].

A precise examination of the microstructure resulting from electrolyte composition is needed to better predict the corrosion behavior in biological conditions. In this study, we compare the effects of different phosphate-based electrolytes, offering insights into the development of the PEO coating layer on a Mg-Ca alloy, with a particular focus on micrometric defects, microstructure, and phase formation, in relation to the coating degradation behavior. Scanning electron microscopy (SEM) is used to measure the thickness of the oxide layer and to track the evolution of its morphology. Analysis of the coating's phase composition using X-ray diffraction (XRD) and transmission electron microscopy (TEM) reveals a multi-phase system that transforms from a crystalline to an amorphous state. Atom probe tomography (APT) is used to quantify the phase composition and to resolve the 3D structure of the nanoscale defects within the coating. Results from TEM and APT help identify the various layers in the coating before and after corrosion, and clarify how the microstructure influences the degradation behavior. Our findings improve our understanding of the coating formation and could lead to the design of PEO coatings with enhanced corrosion resistance. In this work, we test the hypothesis that electrolyte composition governs nanoscale defect chemistry in PEO coatings, thereby controlling degradation pathways. Specifically, we assess (i) how electrolyte chemistry influences phase composition and defect structure, and (ii) how these features determine corrosion initiation and propagation.

2. Methods

2.1. Materials and processing method

The substrate material, ultra-high purity (UHP) Mg-0.45 wt. % Ca alloy, was fabricated and prepared by Kairos Medical AG, Bettlach, Switzerland. Ultra-high purity magnesium (≥ 99.999%, except Zn) was first obtained via distillation of commercially available feedstock. An alloy billet was subsequently produced by adding high-purity calcium (≥ 99.95%) at 750°C under a protective argon atmosphere. Following an 8 h solution heat treatment at 450°C and water quenching, the material was subjected to indirect extrusion at 313°C to form a 7 mm diameter rod (1:55 extrusion ratio), yielding a homogeneous microstructure. Cylindrical specimens (5.5 mm diameter, 12 mm length) were machined from the extruded rods. A second alloy billet, prepared identically, was extruded indirectly at 355°C to yield a bar with a rectangular cross-section of 9 mm× 3.5 mm (1:69 extrusion ratio). From this material, rectangular specimens (8 mm length, 3.5 mm width, 0.3 mm thickness) were machined. Prior to coating, the specimens were ultrasonically cleaned in ethanol in two consecutive 3 min steps. The PEO treatment was performed using a DC electrical source (rectifier MUNK psp family, E230 G500, Munk GmbH, D-59069 Hamm, Germany) in two alkaline electrolytes: (a) diammonium hydrogen phosphate $(NH_4)_2HPO_4$ (6.6 g/L) + urea CH_4N_2O (60 g/L) + ammonia NH_4OH (29.4 g/L), called "A-electrolyte" and (b) KOH (2 g/L) + Na_3PO_4 (10 g/L), called "Na-electrolyte". Hereafter, coatings formed in the A- and Na-electrolytes are referred to as PEO-A and PEO-Na, respectively; all specimen designations are summarized in Table 1. The coatings were obtained at a constant current density of 14 mA/cm^2, with the applied voltage limited to 400 V. The voltage was adjusted in each electrolyte (320 V for PEO-A and 285 V for PEO-Na) to obtain comparable coating thicknesses of approximately 2–3 μm for the initial PEO-A vs. PEO-Na comparison. For this comparison, PEO-A (320 V) and PEO-Na (285 V) coatings were produced on rectangular specimens. To investigate the effect of voltage on coating thickness and structure, an additional PEO-A coating was produced at 390 V on cylindrical specimens. These PEO-A (390 V) coatings were subsequently used for corrosion testing and are denoted as PEO-A + CORR.

2.2. Material characterizations

2.2.1. X-ray diffraction

The structure of the phases present within the coating was assessed using XRD with a Bruker X-ray diffractometer with Cu Kα radiation at an incidence angle of 0.75°, i.e., in a grazing incidence X-ray diffraction (GI-XRD) configuration. The XRD data was analyzed using MDI Jade software (version 9.4). The theoretical X-ray penetration depth was calculated with the Bruker AbsorbX software using the Cu-Kα radiation source in symmetrical scan mode and a MgO density of 3.58 g·cm^{-3}.

2.2.2. Scanning electron microscopy

A 5-10 nm carbon coating was first sputtered onto PEO-coated specimens to minimize surface charging induced by the electron beam. The surface morphology of the specimens was then characterized by secondary electron (SE) using SEM (ZEISS Merlin) at an acceleration voltage of 5 kV and a current of 1 nA. Platinum (Pt) was deposited on the specimen surface using a gas-injection system inside an SEM equipped with a focused ion beam (SEM-FIB) (FEI Helios Nanolab 600i) at an accelerating voltage of 3.0 kV and a current of 1.4 nA. The cross-section morphology was imaged using SEM (ZEISS Merlin) at an acceleration

Table 1
The specimen designation, alloy composition, electrolyte, voltage and corrosion conditions.

Specimen designation	Alloy composition [wt. %]	Electrolyte	Voltage	Corrosion testing
Mg-0.45Ca (PEO-A)	Mg-0.45Ca	$(NH_4)_2HPO_4$ (6.6 g/L) + CH_4N_2O (60 g/L) + NH_4OH (29.4 g/L)	320 V	-
Mg-0.45Ca (PEO-Na)	Mg-0.45Ca	KOH (2 g/L) + Na_3PO_4 (10 g/L)	285 V	-
Mg-0.45Ca (PEO-A) + Corr	Mg-0.45Ca	$(NH_4)_2HPO_4$ (6.6 g/L) + CH_4N_2O (60 g/L) + NH_4OH (29.4 g/L)	390 V	yes

voltage of 2-3 kV and a current of 1 nA. The coating thickness, porosity, crack length density, and delaminated area fraction were calculated through SEM cross-section image analysis in ImageJ (version 1.54j) [24].

2.2.3. Transmission electron microscopy

The lamella extracted was characterized using a TEM (JEOL JEM 2100 Plus) equipped with an Energy Dispersive X-ray Spectroscopy (EDS) detector. The microscope was operated at 200 kV for TEM and scanning (S)TEM imaging. High-angle annular dark field (HAADF) in STEM was performed with a camera length of 20 cm, and SAED patterns were collected using a selected-area aperture with a diameter of approximately 10 μm.

2.2.4. Atom probe tomography

The specimen was manually cleaved to expose the interface between the substrate and coating. The exposed surface of the specimen was mounted in epoxy, ground on SiC papers P400 – P2500, polished with a 3 μm/1 μm diamond suspension, and a final polishing stage using oxide polishing suspension. Two lamellae were prepared by SEM-FIB along the transverse direction and the longitudinal direction, as shown in Fig. S1. This geometry was selected to capture both the coating cross-section and the coating/substrate interface, which are essential for interpreting the microstructural and compositional gradients discussed below. The lamellae prepared as described above were mounted onto flat-top Microtip™ Coupons (PSM M22, Cameca Instruments / Ametek) and were sharpened into a needle-like shape with an end-diameter of typically 100 nm for APT. APT is an analytical technique that involves the removal of individual atoms in the form of ions from the surface of needle-shaped samples using an electrostatic field [25]. After APT sample preparation using the protocol described in Ref. [26], one of the samples was coated with chromium (Cr) using *in situ* coating [27]. This metallic cap improved sample yield due to the mechanical stabilization provided by the thin coating.

The sharpened samples were analyzed in the LEAP™ 5000 XR (Cameca Instruments) fitted with a reflectron detector at a laser pulse energy of 60 pJ, a base temperature of 60 K, a repetition rate of 125 kHz, and a detection rate fixed at 5 ions detected per 1000 pulses on average. The reconstructions of all datasets and analyses were performed in Cameca Instruments AP Suite (version 6.3.0.90). For the default reconstruction, the voltage was used to derive the radius of curvature for Mg-0.45Ca $^{(PEO-A)}$, whereas a fixed shank angle with fixed continuity was used for Mg-0.45Ca $^{(PEO-A)+Corr}$ and Mg-0.45Ca $^{(PEO-Na)}$ because of large fluctuations in the applied voltage. Table S1 lists the identities of each labeled peak in the mass spectra of each sample and supports the compositional analysis. In addition, individual elemental maps for Mg, O, and P are provided in Fig. S2 to enable direct assessment of their spatial distributions and to support the statistical reliability of the composite overlay maps. Quantitative compositional analyses were performed on a reconstructed volume with a radius of approximately 5 nm and a height of 10 nm.

2.2.5. Electrochemical impedance spectroscopy

Electrochemical impedance spectroscopy (EIS) measurements were performed using a BioLogic SP-200 potentiostat/galvanostat (BioLogic Science Instruments, France) in a conventional three-electrode cell containing Hank's balanced salt solution (HBSS; Sigma-Aldrich, Cat. No. H8264-1L). The PEO-coated specimens served as the working electrode, while platinum and Ag/AgCl electrodes were used as the counter and reference electrodes, respectively. Before measurement, the specimens were immersed in the electrolyte until a stable open-circuit potential (OCP) was reached. EIS spectra were recorded at the OCP over a frequency range of 100 kHz to 10 mHz using a sinusoidal perturbation amplitude of 10 mV. The impedance data were fitted with equivalent electrical circuits using EC-Lab software (BioLogic Science Instruments, France).

2.2.6. Statistical methods

The average coating thickness and its standard deviation (±) were determined from measurements at seven distinct locations in the SEM data. In the APT line profiles, the standard deviation of each element's concentration is reported for every bin.

2.3. In vitro degradation testing

In vitro degradation testing was carried out by immersing the test cylinders in 200 mL of Hank's Balanced Salt Solution ((1X), Gibco, REF 14025) at 37°C. After 8 days, the specimen was removed, rinsed with ethanol, and dried at 60°C for 2 hours.

3. Results

3.1. PEO coating via A-electrolyte

GI-XRD of the Mg-0.45Ca $^{(PEO-A)}$ coating prepared in an ammonia-based electrolyte (Fig. 1a) reveals a broad peak at the lower diffraction angle, typical of an amorphous phase. Additional crystalline peaks corresponding to Mg and MgO are also present. The theoretical X-ray penetration depth in MgO ($2\theta = 42.9°$) is 3 μm. Fig. 1b presents the SEM image of the substrate and coating. The average thickness and coating porosity calculated from the cross-section SEM image in Fig. 1b are 2.55 ± 0.38 μm and 8.28%, respectively. Since the theoretical penetration depth for MgO is approximately 3 μm, which is greater than the coating thickness, the majority of the Mg phase detected stems from the Mg-based substrate below the coating.

HAADF-STEM and STEM-EDS mapping of the coating and the substrate cross-section are depicted in Fig. 1c, showing an O-, Mg-, and P-rich coating and a Ca-rich nanoparticle (marked by red arrows) in both the coating and the Mg-rich substrate. The agglomeration of alloying elements directly at the coating/substrate interface and within the coating, as observed in Fig. 1c, has also been reported in previous studies of coated Mg-Ag alloys [28,29]. Ca enrichment is achieved through the preferential oxidation of the Mg matrix, which has a higher corrosion potential (-2.37 VSCE) than the Mg_2Ca phase (-1.54 VSCE) [5]. A similar phenomenon was also observed in the Mg-Zn-Ca alloy immersed in a simulated body fluid (SBF) solution for up to nine days [30]. The undissolved Ca can be incorporated into the coating under the applied electric field during the coating process. Further analysis of the cross-section microstructure by bright-field TEM (Fig. 1d) reveals an approximately 100–200 nm thick layer between the substrate and the coating. Selected area electron diffraction (SAED) patterns suggest that the thin anodic layer is dense and comprises the MgO phase, as indicated by the strong intensity of the ring-pattern and diffraction spots. The inner layer is porous and partly amorphous, as evidenced by the diffuse rings. This layer also includes polycrystalline MgO; however, the intensity of the ring-pattern and diffraction spots is reduced compared to the anodic layer. The outer layer is likely more amorphous in nature than the preceding layers, owing to the weaker intensity of the diffraction spots and the diffuse ring-pattern.

The microstructure of the Mg-0.45Ca $^{(PEO-A)}$ inner and outer coating layers can be explained by their distinct chemical compositions, as revealed by APT. The reconstruction of the outer coating layer reveals a uniform distribution of O, Mg, P, H, and Ca depicted in Fig. 2a. It is not readily apparent whether H originates from the coating, as the observed levels of H are consistent with the baseline levels that can be detected from residual gases [31]. The 1D concentration profile along the depth of this region (Fig. 2b) indicates that the coating is a single phase primarily composed of 46 at. % O, 36 at. % Mg, and 15 at. % P. The remaining 3 at. % comprising all other detected species, including H and Ca, was excluded from the reported composition.

APT reconstruction of the coating and substrate interface in Fig. 2c reveals distinct chemical and structural features across the anodic layer, interface, and substrate. The anodic layer near the coating interface

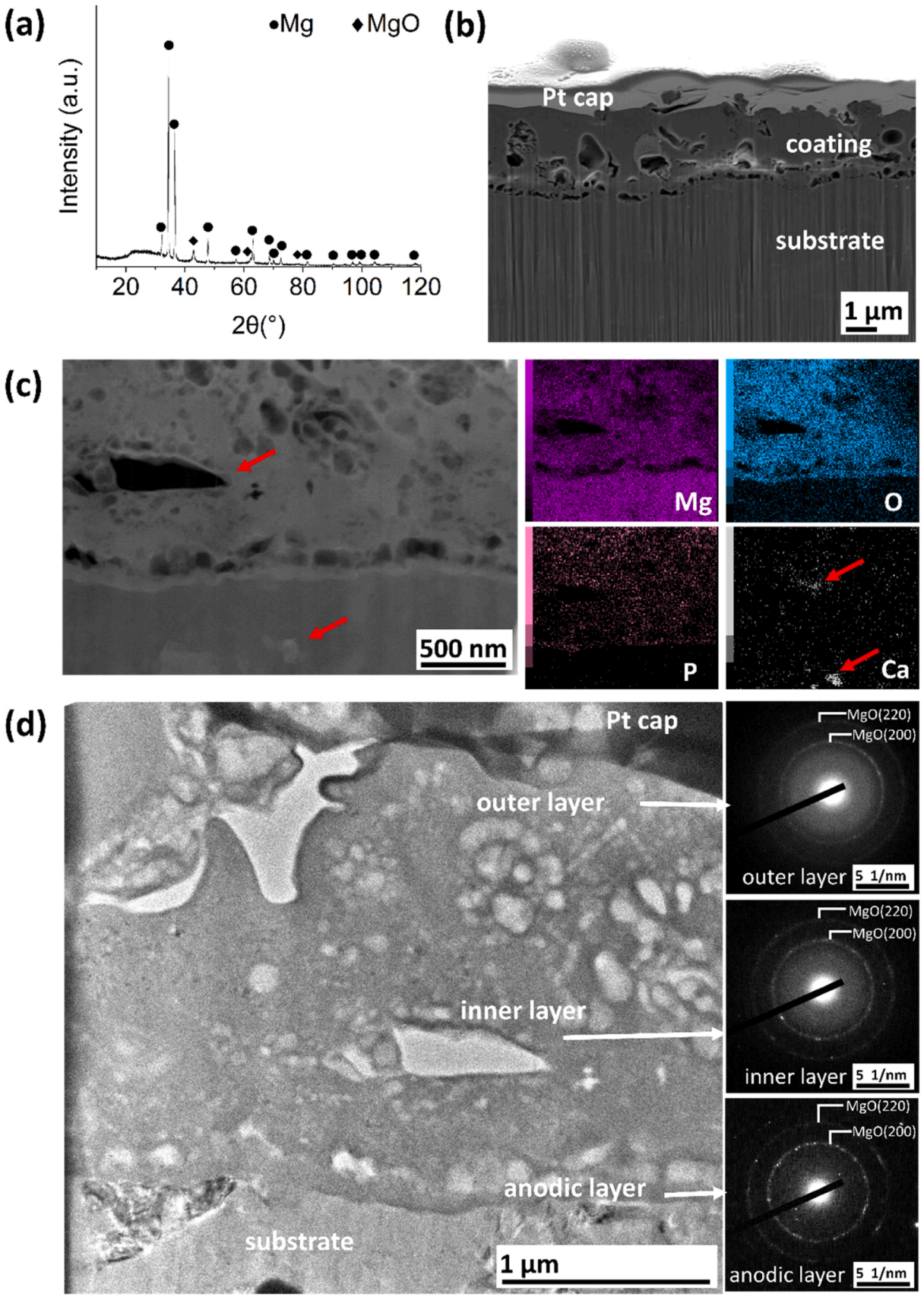

Fig. 1. Mg-0.45Ca $^{(PEO\text{-}A)}$ specimen: (a) GI-XRD, (b) SEM image of coating cross-section, (c) STEM/EDS elemental maps of the coating cross-section (Ca-rich nanoparticles are marked by red arrows), and (d) TEM image of coating cross-section and selected-area electron diffraction (SAED) patterns.

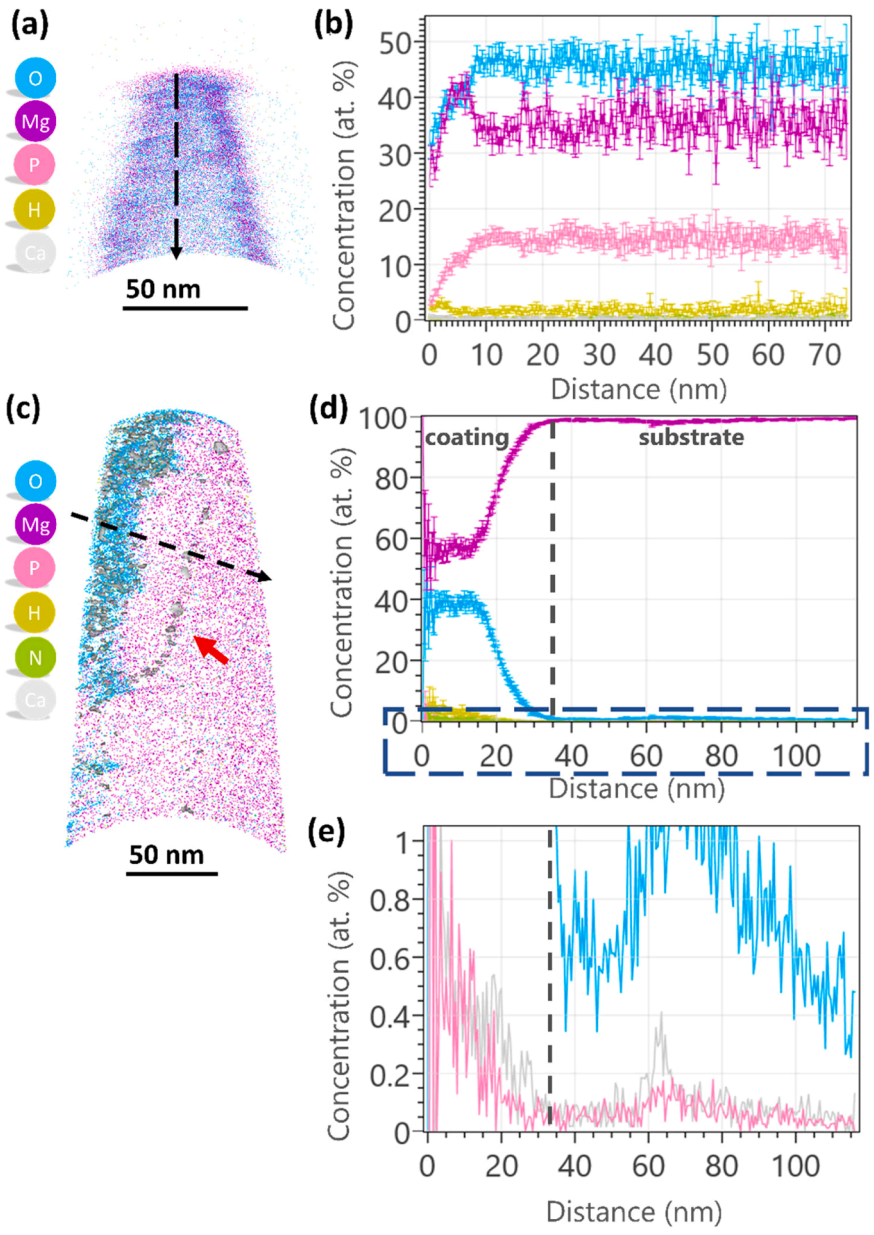

Fig. 2. APT analysis of the Mg-0.45Ca $^{(PEO-A)}$ specimen: (a) 2D slice of the outer coating layer along a representative xz plane revealing the elemental distributions of O, Mg, P, H, and Ca, (b) corresponding line profile, (c) 2D slice of the coating–substrate interface along a representative yz plane revealing the elemental distributions of O, Mg, P, H, N and Ca, with Ca nanoparticles represented by the 0.6 at. % Ca isoconcentration surface in a Mg matrix, (d) corresponding line profile across the interface between the coating and the substrate, highlighting the interfacial localization of N, and (e) close-up view of the region in (d) indicated by the dashed rectangle. The error bars represent variation within the single line profile measurement.

(Fig. 2d) has a composition of ~34 at. % O, 63 at. % Mg and 3 at. % comprising all other detected species, including H, Ca, and N. Considering previous reports of compositional inaccuracies in stoichiometric MgO measurements [32,33], (often due to the formation of non-detectable neutral O_2 molecules [34]), we interpret this phase as MgO. N is localized at the coating/substrate interface and is not detected in the outer coating layer. The interfacial localization suggests that N is incorporated during coating formation rather than being uniformly distributed within the coating. However, the present data does not allow a definitive assignment of the nitrogen chemical state. The substrate adjacent to the coating contains approximately 99 at. % Mg and Ca, in the form of nanoscale Ca clusters, as evidenced by the composition profile in Fig. 2e. These particles are confined to the Mg substrate and shown by a set of isoconcentration surfaces, which are visualization tools that show where the local Ca concentration exceeds 0.6 at. %, as shown in Fig. 2c.

3.2. *In vitro degradation behavior*

Comparative images, including cross-sections, were obtained from two specimens before and after in vitro degradation. Before *in vitro* testing, the surface morphology of the Mg-0.45Ca $^{(PEO-A)+Corr}$ specimen showed an inhomogeneous distribution of pores and uneven texture, as seen in the backscattered-electron image in Fig. 3a. The SEM cross-section image in Fig. 3b reveals a porous coating with a relatively dense outer layer. The average coating thickness of the Mg-0.45Ca $^{(PEO-A)+Corr}$ (390 V) sample was initially 7.00 ± 1.21 μm, compared with 2.55 ± 0.38 μm for the Mg-0.45Ca $^{(PEO-A)}$ (320 V) sample (Fig. 1b). These differences reflect the effect of applied voltage (320 V vs. 390 V) on coating growth. The increase in thickness with increasing voltage is

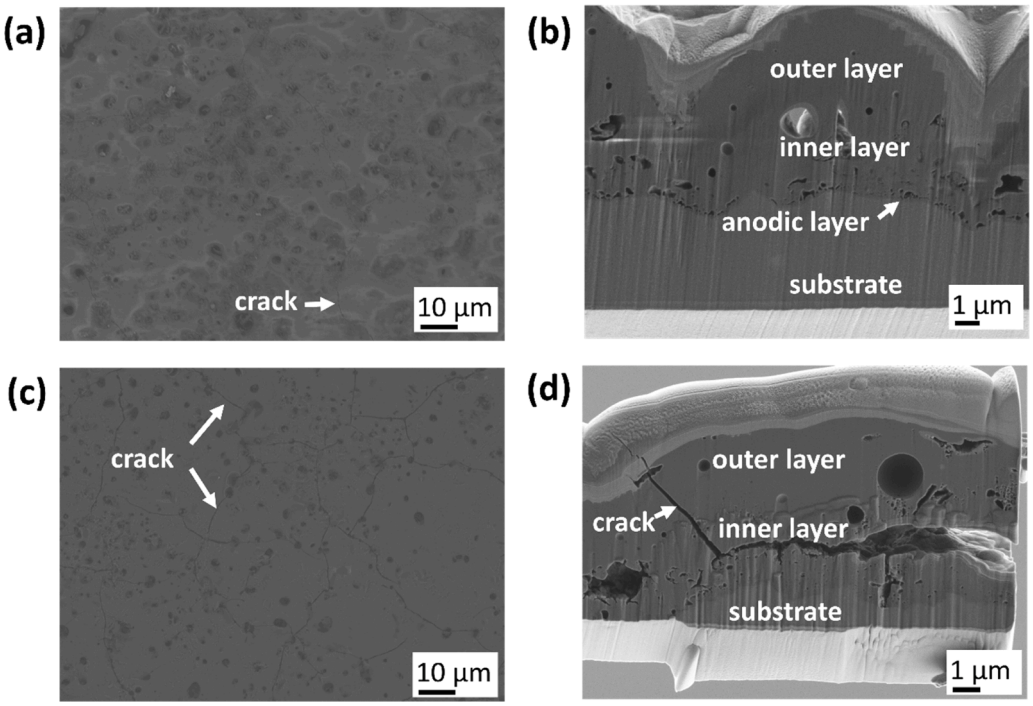

Fig. 3. Surface morphology and cross-sectional morphologies of the Mg-0.45Ca $^{(PEO-A)}$ specimen (a-b) before, and (c-d) after immersion in HBSS solution at 37°C for 8 days.

consistent with the expected voltage-dependent growth of PEO coatings [17,18]. Following *in vitro* testing, the Mg-0.45Ca $^{(PEO-A)\ +\ Corr}$ specimen showed visible changes in the surface morphology. Although the coating remained generally uniform, the surface exhibited a markedly increased density of pores and cracks, as shown in Fig. 3c. The crack length density increased from approximately 33.77 mm^{-1} before corrosion to 106.05 mm^{-1} after corrosion. The cracks are seen to propagate through the outer layer and terminate in the inner layer, where delamination is observed in Fig. 3d. The delaminated area fraction was 6.24%. We determined the average coating thickness to be 5.49 ± 0.43 µm, corresponding to an average reduction of 21.6%.

According to APT analysis, the outer coating layer of the Mg-0.45Ca $^{(PEO-A)\ +\ Corr}$ after immersion testing is composed of O, Mg, P, and H, as shown in the 3D atom map and the concentration profiles in Fig. 4a-b. The bulk coating is composed of 55 at. % O, 28 at. % Mg, and 16 at. % P. There is an enrichment of 10–12 at. % H in the topmost 10 nm, dropping rapidly to the bulk coating composition. Measuring H content by APT is known to be challenging because of the presence of residual H within the instrument's ultrahigh vacuum chamber and possibilities of introduction during sample preparation and transport [31]. However, the accompanying change in the composition of the other elements allows us to conclude that this top layer is a metastable reaction product of the bulk coating and HBSS.

Further analysis of the inner layer in Fig. 4c reveals an inhomogeneous distribution of elements and H enrichment highlighted by a set of isoconcentration surfaces with a threshold of 3 at. % H. Variations in the voltage curve during APT analysis (Fig. S3) are indicators of local curvature of the sample's surface. Such variations can arise from phase-dependent evaporation fields, which distort ion trajectories near interfaces and generate local magnification artifacts in APT reconstructions [35]. To examine these variations in more detail, 2D maps of the local point density were calculated and plotted within 2-nm-thick slices marked by the black square and dotted black square displayed in Fig. 4d and 4e, respectively. In Fig. 4d, a particularly high point density was measured on the left side of the reconstruction, and the corresponding concentration profile shows a P enrichment, supporting the idea that these point density variations are related to changes in composition. In contrast, the opposite side of the APT sample, composed of 55 at. % O and 45 at. % Mg corresponds to the region with a relatively low point density, suggesting that MgO has a higher evaporation field compared to P-enriched regions. In Fig. 4e, the point density variations are more pronounced, extending into the core of the sample, as marked by a red arrow. Together with the concentration profile, these features are interpreted as a set of H-filled pores, whose inner surfaces, marked by the vertical lines in the profile, are enriched in Mg, O, and P. The Mg, O, and P ions detected within the pore core are therefore not attributed to the pore interior itself. This interpretation is consistent with the report by Wang et al., who showed that 90% or more of the atoms in concentration profiles across voids in NiCoCr are from the pore's interior surfaces [36]. The corrosion-induced degradation, inferred from the clear morphological changes observed by SEM after corrosion, is further supported by the APT results, although no Na or Cl is detected in the pores.

3.3. PEO coating via Na-electrolyte

The Mg-0.45Ca $^{(PEO-Na)}$ coating prepared in a Na-containing electrolyte also exhibits a mixed-phase structure. GI-XRD of the Mg-0.45Ca $^{(PEO-Na)}$ coating (Fig. S4) reveals a broad peak and additional reflections corresponding to amorphous material, MgO, and Mg. The specimen surface is characterized by pores and cracks as seen in Fig. 5a. The average thickness and coating porosity from the cross-section SEM image of the coating in Fig. 5b are 2.01 ± 0.17 µm and 3.0%, respectively. Ca, the alloying solute element from the substrate, is present as precipitates, mainly in the coating containing O, P, and Mg near the Mg substrate, as shown in the STEM-EDS maps in Fig. 5c. TEM imaging of the cross-section of the coating in Fig. 5d reveals a dense outer layer and a porous inner layer. The inner layer is polycrystalline as indicated by the intense ring-pattern and specific bright spots, while SAED patterns from the middle region of the coating display both amorphous and polycrystalline structures. However, the reduction in the intensity of the ring pattern suggests that the amorphous structure is more pronounced in the outer layer than in the inner layer.

The APT reconstruction of the outer coating layer reveals a

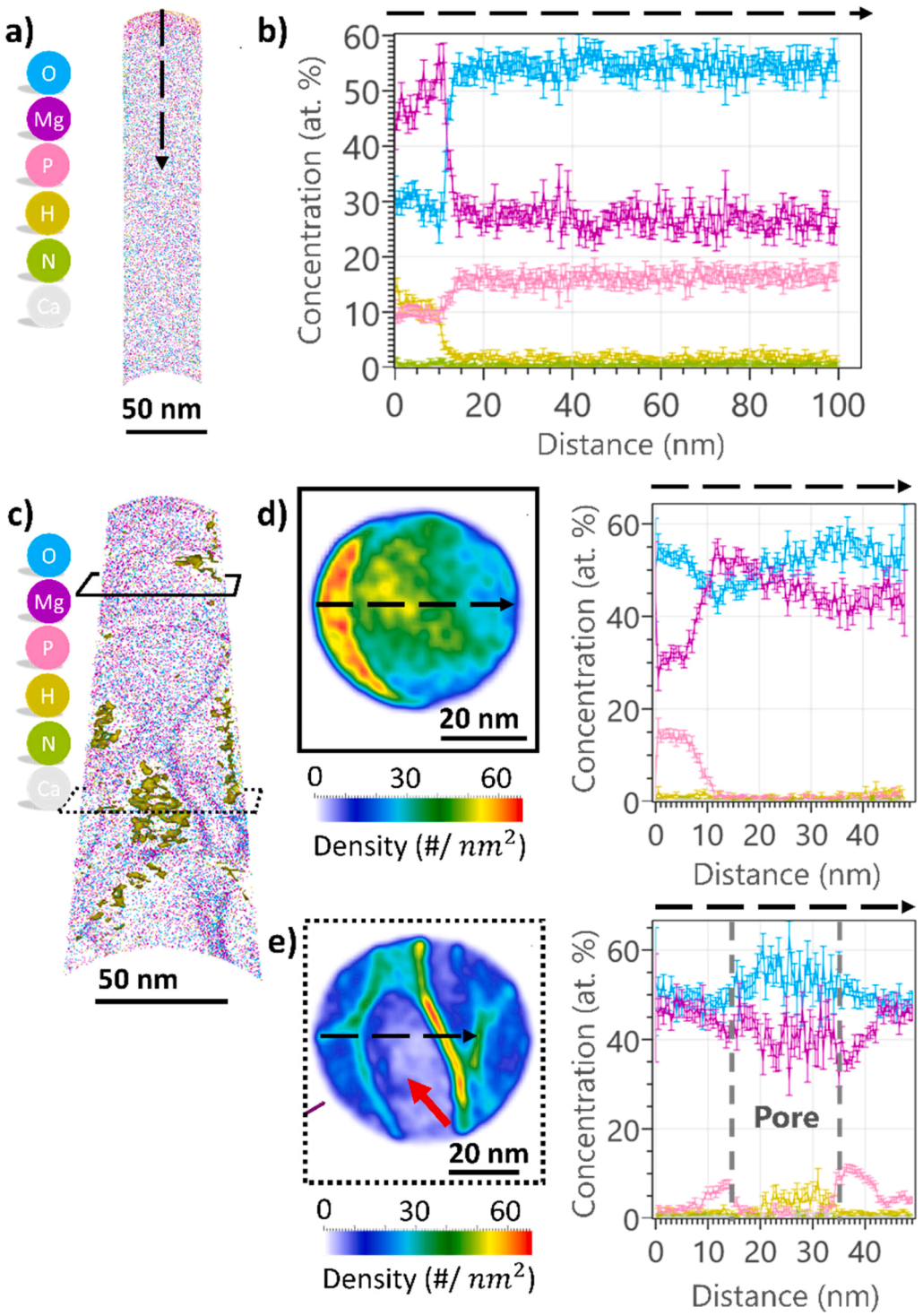

Fig. 4. APT analysis of the Mg-0.45Ca $^{(PEO\text{-}A)\ +\ Corr}$ after immersion testing. (a) 2D slice of the outer coating layer along a representative yz plane revealing O, Mg, P, H, N and Ca elemental distribution, (b) corresponding line profile, (c) 2D slice of the inner coating layer along a representative yz plane showing H enrichment (3 at. % H isoconcentration surface) in porous regions, (d) 2D density plot (of the region in c indicated by the solid rectangle) and corresponding line profile across dashed line, and (e) 2D density plot (of the region in c indicated by the dotted rectangle) and corresponding line profile across dashed line. The error bars represent variation within the single line profile measurement.

heterogeneous distribution of O, Mg, P, H, and Na depicted in Fig. 6a. The 1D concentration profile along the dashed line in Fig. 6b shows that the coating consists of two distinct compositions delineated by high H concentrations. Although the inner coating layer also contains O, Mg, P, H, and Na, as seen in Fig. 6c, there is a notable change in porosity and Na segregation. In Fig. 6d, the 2D density plot of the region, denoted by the solid rectangle, shows a low-density region (marked by a red arrow) that can likely be ascribed to pores, as discussed above. A concentration profile (Fig. 6e), acquired across the dense-coated region, indicates an enrichment of Na up to 19 at. % due to the defects within the microstructure.

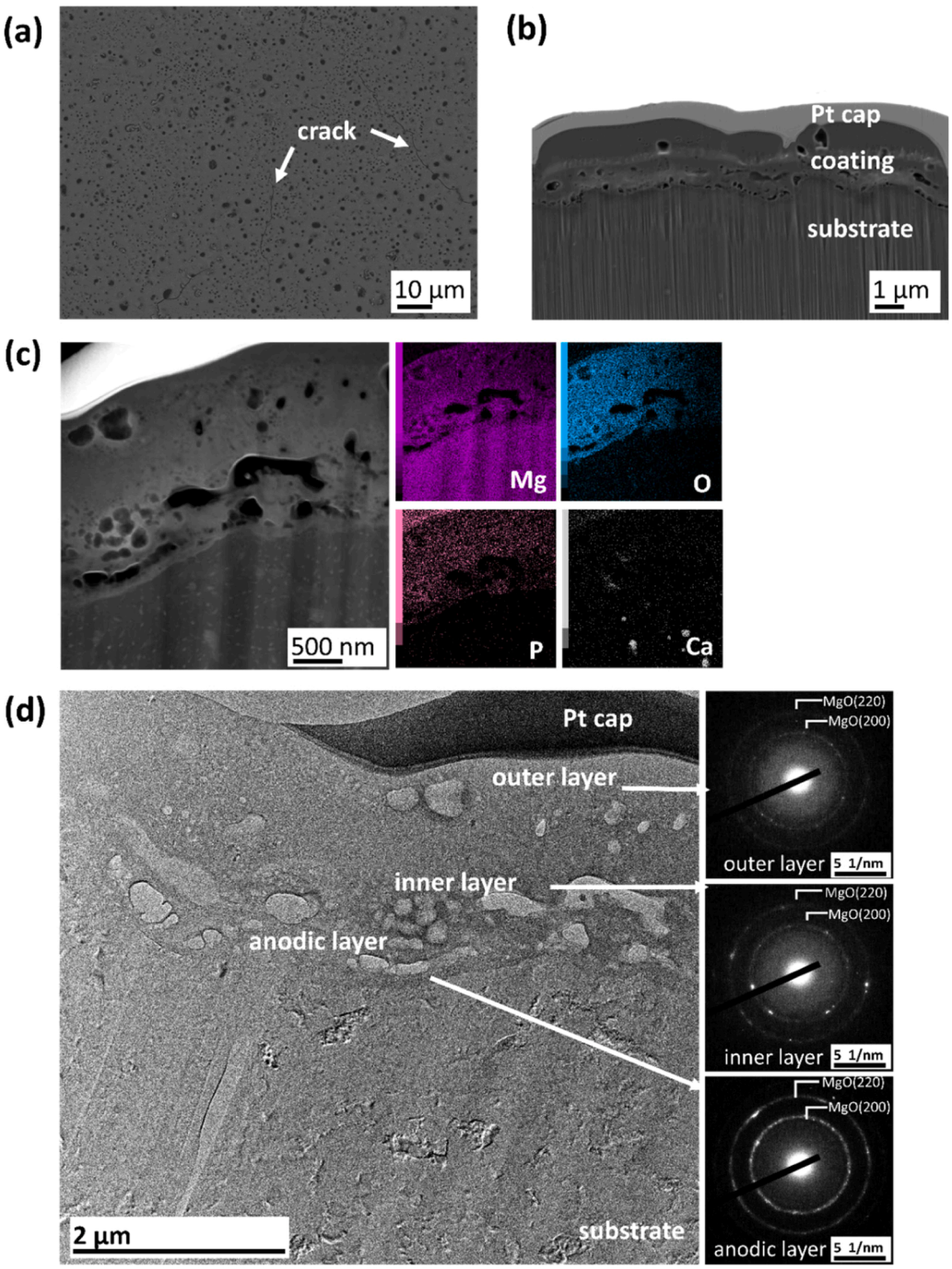

Fig. 5. Mg-0.45Ca $^{(PEO\text{-}Na)}$ specimen: (a) SEM image of coating surface, (b) SEM image of coating cross-section, (c) STEM/EDS elemental maps of coating cross-section, and (d) TEM image of coating cross-section and selected-area electron diffraction (SAED) pattern.

4. Discussion

4.1. Microstructural evolution

Previous studies of the microstructure of PEO-coated Mg-based alloys have been plagued by contradictory observations, including the absence of an amorphous P-rich phase detected by XRD yet revealed by EDS analysis in Mg-0.45Ca [23]. SEM, TEM, and APT analyses presented here reconcile this discrepancy by revealing nanoscale P-rich regions that are predominantly amorphous and therefore below the detection limit of GI-XRD. These observations provide further insight into the growth mechanism of the PEO coating. During the initial exposure of the Mg alloy to the electrolyte, Mg is oxidized to Mg^{2+} and reacts with oxygen/hydroxide species, to form a thin, compact crystalline MgO layer. The presence of this layer indicates that the early stage of PEO growth is dominated by anodic oxidation and barrier-layer formation, consistent with previous reports of 10-20 nm oxide layers formed during the early stages of Mg oxidation [37–39].

With continued anodization and the onset of plasma discharges, the growth mechanism shifts from barrier-layer formation to plasma-assisted incorporation of electrolyte species. Once a dense anodic layer is formed, ion uptake from the electrolyte governs the subsequent growth stages, leading to the formation of a P-rich phase (15-16 at. % P) together with MgO in both inner and outer layers. The PO_4^{3-} anions present in the Na_3PO_4 electrolyte enable the formation of $Mg_3(PO_4)_2$ in

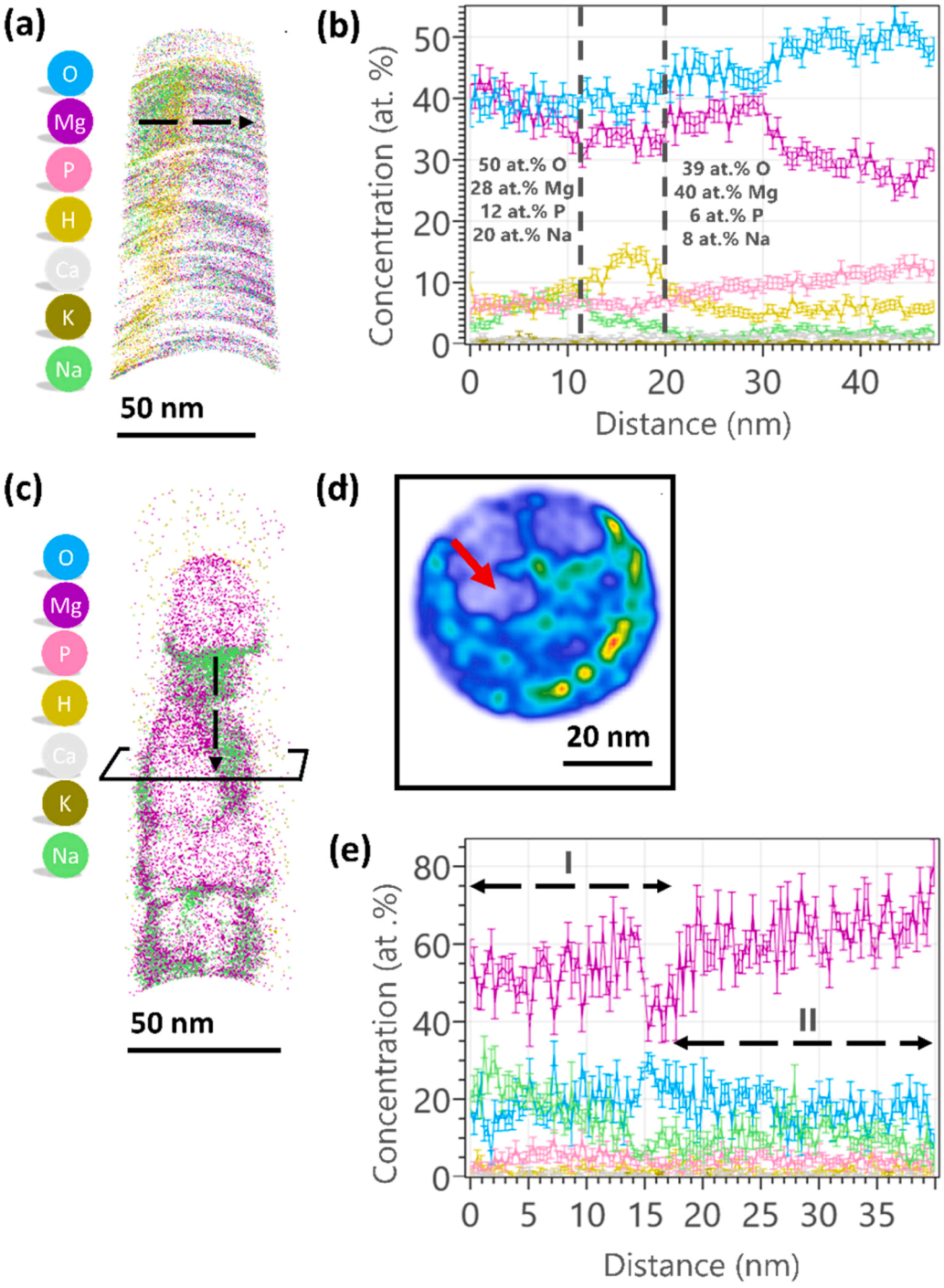

Fig. 6. APT analysis of the Mg-0.45Ca $^{(PEO\text{-}Na)}$ specimen. (a) 2D slice of the outer coating layer along a representative yz plane revealing O, Mg, P, H, K and Na elemental distribution, (b) corresponding line profile, (c) 2D slice of the inner coating layer along a representative yz plane showing Na enrichment and porous regions, (d) 2D density plot (of the region in c indicated by the solid rectangle) showing low point density region (marked by a red arrow) and (e) corresponding line profile across dashed line. The error bars represent variation within the single line profile measurement.

addition to the MgO phase within the PEO coatings [40]. However, the P-rich phase observed here, in contrast to the crystalline phase previously reported by Ghasemi et al. [40], suggests that crystallization is suppressed by the relatively low current density (14 mA/cm^2) used here, which produces lower-energy plasma discharges and rapid cooling. At higher current densities, greater discharge energy and slower cooling within thicker coatings can promote crystallization [41]. This could explain why the P-rich phase that formed at lower current densities did not transition from an amorphous to a crystalline state.

The predominantly amorphous nature of the P-rich phase also explains the inconsistent identification of $Mg_3(PO_4)_2$ in prior EDS and XRD studies [40,42–44]. While EDS can detect local P enrichment, GI-XRD is insensitive to nanoscale or amorphous phases. The present results therefore support a non-equilibrium growth mechanism in which electrolyte species are incorporated during plasma discharge events and rapidly solidified before significant crystallization can occur. Mg-0.45Ca $^{(PEO\text{-}Na)}$ $^{(PEO\text{-}A)}$ coatings exhibit a three-tier cross-section similar to Mg-0.45Ca coatings, consisting of crystalline MgO and P-rich phase, as confirmed by SEM/TEM observations, XRD phase analysis and APT compositional analysis. APT results (Fig. 6b) show limited Na

incorporation (1–2 at. %), suggesting that Na^+ is incorporated only to a minor extent into the P-rich phase because of charge and size mismatch with Mg^{2+} vacancies [45]. Instead, excess Na^+ segregates to pore walls (Fig. 6c–d), consistent with transport through discharge channels and subsequent rejection during rapid solidification. This supports a two-stage PEO growth mechanism: initial formation of a crystalline MgO barrier layer, followed by plasma-assisted incorporation of electrolyte species and rapid solidification, producing nanoscale, predominantly amorphous P-rich regions. The final coating microstructure is therefore governed by the interplay between electrolyte chemistry, plasma discharge energy, and cooling rate.

4.2. Microstructure-controlled in vitro degradation

A key challenge in understanding and predicting the degradation behavior of PEO coatings is establishing how electrolyte-ion exchange affects their corrosion resistance. As an initial indication, EIS measurements were performed on the as-coated specimens; the corresponding Nyquist and Bode plots, equivalent-circuit model, and fitted parameters are provided in Fig. S5 and Table S2. The Mg-0.45Ca $^{(PEO\text{-}A)}$ coating exhibited higher inner- and outer-layer coating resistances than the Mg-0.45Ca $^{(PEO\text{-}Na)}$ coating, consistent with its higher impedance response under the tested conditions. However, time-resolved impedance measurements during prolonged immersion would be required to quantify the evolution of coating barrier properties and degradation kinetics.

The microstructural features identified above provide a basis for understanding the subsequent in vitro degradation behavior of the Mg-0.45Ca $^{(PEO\text{-}A)}$ coating. Following immersion, new cracks developed at the surface and extended to depths of up to 5 μm within the Mg-0.45Ca $^{(PEO\text{-}A)+Corr}$ coating (Fig. 3c-d). These surface cracks were accompanied by local volume changes likely associated with corrosion product formation and hydroxylation of the amorphous phase. Such microstructural changes may promote electrolyte ingress and further accelerate local degradation, potentially contributing to the delamination observed at the inner layer.

Despite a reduction in total coating thickness of more than 20%, the dense morphology of the outer layer remained largely unchanged after corrosion (Fig. 4a), suggesting relatively uniform dissolution of this region. In contrast, the inner layer developed a pronounced mesh-like morphology indicative of heterogeneous degradation (Fig. 4b). This difference is consistent with the distinct phase compositions of the two layers: the outer layer has a substantially lower Mg/(P+O) atomic ratio and a higher fraction of P-rich amorphous material, whereas the inner layer is comparatively enriched in crystalline MgO. The lower stability of the P-rich phase relative to crystalline MgO in chloride-containing aqueous environments may therefore promote preferential dissolution of the inner layer [41,46].

Previous studies of PEO-coated Mg alloys have similarly reported preferential dissolution of unstable amorphous constituents during the initial interaction with HBSS, followed by redeposition of relatively insoluble corrosion products [47]. Accordingly, the heterogeneous degradation observed here may result from preferential dissolution of the P-rich phase, although its specific thermodynamic and kinetic stability were not directly evaluated in this study. As degradation proceeds, progressive removal of the less stable P-rich phase would increase the relative fraction of the more corrosion-resistant MgO, potentially reducing the subsequent degradation rate of the inner layer.

5. Conclusion

While phosphate-based PEO coatings on Mg-0.45Ca are known to reduce early H_2 evolution, this study demonstrates that their long-term performance hinges on degradation behavior controlled by nanoscale heterogeneities that act as preferential corrosion initiation sites due to their intrinsic nanoporosity and lower stability in simulated body fluids. Contrary to prior assumptions of uniform coating degradation, our results reveal a defect-driven mechanism in which H-enriched reaction layers promote localized attack. The pronounced Na segregation at pore walls suggests that Na-containing systems may be particularly susceptible. While these findings are based on short-term *in vitro* testing, they highlight the importance of evaluating degradation under more physiologically relevant conditions. Ultimately, improving coating performance requires controlling the phase distribution and defect network that promote localized attack, providing a pathway for designing PEO coatings, with further validation needed under extended *in vitro* and *in vivo* conditions.

Data availability

All data needed to evaluate the conclusions in the paper are included in the paper and/or supplementary materials. Additional data for this work can be requested from the contributing authors.

CRediT authorship contribution statement

Selase Torkornoo: Writing – original draft, Visualization, Validation, Methodology, Investigation, Formal analysis, Data curation, Conceptualization. **Eric Woods:** Writing – review & editing, Investigation, Formal analysis. **Yongqiang Kang:** Writing – review & editing, Investigation, Formal analysis. **Raymond Kwesi Nutor:** Writing – review & editing, Formal analysis. **Qiuying Ji:** Investigation. **Leopold Berger:** Writing – review & editing, Validation, Resources. **Thomas Imwinkelried:** Writing – review & editing, Validation, Resources. **Baptiste Gault:** Writing – review & editing, Supervision, Project administration, Investigation, Funding acquisition, Formal analysis.

Declaration of competing interest

The authors declare that they have no known competing financial interests or personal relationships that could have appeared to influence the work reported in this paper.

Acknowledgements

This research was supported by Deutsche Forschungsgemeinschaft (DFG) for funding through Baptiste Gault's Leibniz Award. The authors would also like to acknowledge the contributions of Uwe Tezins, Andreas Sturm, Christian Broß, Katja Angenendt, Stefan Zaefferer, Benjamin Breitbach, Volker Kree, and Adrian Savovici for their support of the metallography, XRD, SEM, FIB, TEM, and APT facilities at the Max Planck Institute for Sustainable Materials.

Supplementary materials

Supplementary material associated with this article can be found, in the online version, at doi:10.1016/j.actbio.2026.10.022.

References

[1] J. Walker, S. Shadanbaz, T.B.F. Woodfield, M.P. Staiger, G.J. Dias, Magnesium biomaterials for orthopedic application: a review from a biological perspective, J. Biomed. Mater. Res. B: Appl. Biomater. 102 (2014) 1316–1331, https://doi.org/10.1002/jbm.b.33113.
[2] M.P. Staiger, A.M. Pietak, J. Huadmai, G. Dias, Magnesium and its alloys as orthopedic biomaterials: a review, Biomaterials 27 (2006) 1728–1734, https://doi.org/10.1016/j.biomaterials.2005.10.003.
[3] U. Gröber, J. Schmidt, K. Kisters, Magnesium in prevention and therapy, Nutrients 7 (2015) 8199–8226, https://doi.org/10.3390/nu7095388.
[4] F.I. Wolf, A. Cittadini, Chemistry and biochemistry of magnesium, Mol. Asp. Med. 24 (2003) 3–9, https://doi.org/10.1016/S0098-2997(02)00087-0.
[5] W.-C. Kim, J.-G. Kim, J.-Y. Lee, H.-K. Seok, Influence of Ca on the corrosion properties of magnesium for biomaterials, Mater. Lett. 62 (2008) 4146–4148, https://doi.org/10.1016/j.matlet.2008.06.028.
[6] Z. Li, X. Gu, S. Lou, Y. Zheng, The development of binary Mg–Ca alloys for use as biodegradable materials within bone, Biomaterials 29 (2008) 1329–1344, https://doi.org/10.1016/j.biomaterials.2007.12.021.

[7] T. Akhmetshina, L. Berger, I. Basu, S. Montibeller, W. Rubin, A.M. Rich, R. E. Schäublin, J.F. Löffler, High-performance ultra-lean biodegradable Mg–Ca alloys and guidelines for their processing, Acta Mater. 278 (2024) 120247, https://doi.org/10.1016/j.actamat.2024.120247.
[8] J.W. Seong, W.J. Kim, Development of biodegradable Mg–Ca alloy sheets with enhanced strength and corrosion properties through the refinement and uniform dispersion of the Mg2Ca phase by high-ratio differential speed rolling, Acta Biomater. 11 (2015) 531–542, https://doi.org/10.1016/j.actbio.2014.09.029.
[9] H. Pan, G. Qin, Y. Ren, L. Wang, S. Sun, X. Meng, Achieving high strength in indirectly-extruded binary Mg–Ca alloy containing Guinier–Preston zones, J. Alloys Compd. 630 (2015) 272–276, https://doi.org/10.1016/j.jallcom.2015.01.068.
[10] N.T. Kirkland, N. Birbilis, J. Walker, T. Woodfield, G.J. Dias, M.P. Staiger, In-vitro dissolution of magnesium–calcium binary alloys: clarifying the unique role of calcium additions in bioresorbable magnesium implant alloys, J. Biomed. Mater. Res. B: Appl. Biomater. 95B (2010) 91–100, https://doi.org/10.1002/jbm.b.31687.
[11] N. Wang, S. Yang, H. Shi, Y. Song, H. Sun, Q. Wang, L. Tan, S. Guo, Magnesium alloys for orthopedic applications: a review on the mechanisms driving bone healing, J. Magnes. Alloys 10 (2022) 3327–3353, https://doi.org/10.1016/j.jma.2022.11.014.
[12] W. Li, W. Qiao, X. Liu, D. Bian, D. Shen, Y. Zheng, J. Wu, K.Y.H. Kwan, T.M. Wong, K.M.C. Cheung, K.W.K. Yeung, Biomimicking bone–implant interface facilitates the bioadaption of a new degradable magnesium alloy to the bone tissue microenvironment, Adv. Sci. 8 (2021) 2102035, https://doi.org/10.1002/advs.202102035.
[13] H. Ben Amara, J. Philip, O. Omar, P. Thomsen, Gas bubbles from biodegradable magnesium implants convey mechanical cues and promote immune cell stimulation, Adv. Sci. 12 (2025) 2503123, https://doi.org/10.1002/advs.202503123.
[14] G. Li, H. Cui, R. Fan, G. Liu, Z. Hou, Y. Zhang, X. Che, T. Wang, H. Wei, P. Li, Delivery of molecular hydrogen for precision immunomodulation: mechanisms, detection methods, and applications, Adv. Sci. 12 (2025) e00283, https://doi.org/10.1002/advs.202500283.
[15] J. Jin, L. Yue, M. Du, F. Geng, X. Gao, Y. Zhou, Q. Lu, X. Pan, Molecular hydrogen therapy: mechanisms, delivery methods, preventive, and therapeutic application, MedComm 6 (2025) e70194, https://doi.org/10.1002/mco2.70194.
[16] T.S.N. Sankara Narayanan, I.S. Park, M.H. Lee, Strategies to improve the corrosion resistance of microarc oxidation (MAO) coated magnesium alloys for degradable implants: Prospects and challenges, Prog. Mater. Sci. 60 (2014) 1–71, https://doi.org/10.1016/j.pmatsci.2013.08.002.
[17] J. Zhang, Y. Gu, Y. Guo, C. Ning, Electrochemical behavior of biocompatible AZ31 magnesium alloy in simulated body fluid, J Mater Sci 47 (2012) 5197–5204, https://doi.org/10.1007/s10853-012-6403-5.
[18] S. Cheng, R. Wang, C. Peng, Y. He, X. Wang, Z. Cai, Y. Feng, Effect of voltage on microstructure and corrosion resistance of micro-arc oxidation coating on Mg–Zn–Ca biodegradable alloy, J. Mater. Res. Technol. 30 (2024) 3021–3033, https://doi.org/10.1016/j.jmrt.2024.04.042.
[19] G.-H. Lv, H. Chen, L. Li, E.-W. Niu, H. Pang, B. Zou, S.-Z. Yang, Investigation of plasma electrolytic oxidation process on AZ91D magnesium alloy, Curr. Appl. Phys. 9 (2009) 126–130, https://doi.org/10.1016/j.cap.2007.12.007.
[20] Y. Gu, S. Bandopadhyay, C. Chen, Y. Guo, C. Ning, Effect of oxidation time on the corrosion behavior of micro-arc oxidation produced AZ31 magnesium alloys in simulated body fluid, J. Alloys Compd. 543 (2012) 109–117, https://doi.org/10.1016/j.jallcom.2012.07.130.
[21] A. Ghanbari, A. Bordbar Khiabani, A. Zamanian, B. Yarmand, M. Mozafari, The competitive mechanism of plasma electrolyte oxidation for the formation of magnesium oxide bioceramic coatings, Mater. Today: Proc. 5 (2018) 15677–15685, https://doi.org/10.1016/j.matpr.2018.04.178.
[22] A. Kopp, H. Fischer, A.P. Soares, K. Schmidt-Bleek, C. Leber, H. Kreiker, G. Duda, N. Kröger, K. van Gaalen, H. Hanken, O. Jung, R. Smeets, M. Heiland, C. Rendenbach, Long-term *in vivo* observations show biocompatibility and performance of ZX00 magnesium screws surface-modified by plasma-electrolytic oxidation in Göttingen miniature pigs, Acta Biomater. 157 (2023) 720–733, https://doi.org/10.1016/j.actbio.2022.11.052.
[23] L. Berger, S. Dolert, T. Akhmetshina, J.-P. Burkhard, M. Tegelkamp, A.M. Rich, W. Rubin, S. Darwiche, G. Kuhn, R.E. Schäublin, B. von Rechenberg, B. Schaller, K. M. Nuss, J.F. Löffler, *In vivo* performance of lean bioabsorbable Mg–Ca alloy X0 and comparison to WE43: influence of surface modification and alloying content, Bioact. Mater. 44 (2025) 501–515, https://doi.org/10.1016/j.bioactmat.2024.09.036.
[24] C.A. Schneider, W.S. Rasband, K.W. Eliceiri, NIH Image to ImageJ: 25 years of image analysis, Nat. Methods 9 (2012) 671–675, https://doi.org/10.1038/nmeth.2089.
[25] B. Gault, A. Chiaramonti, O. Cojocaru-Mirédin, P. Stender, R. Dubosq, C. Freysoldt, S.K. Makineni, T. Li, M. Moody, J.M. Cairney, Atom probe tomography, Nat. Rev. Methods Primers 1 (2021) 51, https://doi.org/10.1038/s43586-021-00047-w.
[26] K. Thompson, D. Lawrence, D.J. Larson, J.D. Olson, T.F. Kelly, B. Gorman, In situ site-specific specimen preparation for atom probe tomography, Ultramicroscopy 107 (2007) 131–139, https://doi.org/10.1016/j.ultramic.2006.06.008.
[27] T.M. Schwarz, E. Woods, M.P. Singh, X. Chen, C. Jung, L.S. Aota, K. Jang, M. Krämer, S.-H. Kim, I. McCarroll, B. Gault, In situ metallic coating of atom probe specimen for enhanced yield, performance, and increased field-of-view, Microsc. Microanal. (2024), https://doi.org/10.1093/mam/ozae006 ozae006.
[28] Y. Zhang, Y. Lv, B. Liu, X. Cao, X. Ma, T. Hashimoto, S. Wang, Z. Dong, X. Zhang, Incorporation of magnesium phosphate into magnesium oxide on MgAg alloy through plasma electrolytic oxidation, Surf. Coat. Technol. 447 (2022) 128822, https://doi.org/10.1016/j.surfcoat.2022.128822.
[29] X. Zhang, Y. Zhang, Y. Lv, Z. Dong, L. Yang, E. Zhang, T. Hashimoto, X. Zhou, PEO coating on Mg-Ag alloy: the incorporation and release of Ag species, J. Magnes. Alloys 11 (2023) 2182–2195, https://doi.org/10.1016/j.jma.2021.12.006.
[30] S. Meng, K. Liu, Y. Zhang, Z. Tang, J. Liu, P. Zhou, T. Zhang, Y. Zhang, Ł. Maj, F. Wang, A new look into the electrochemical impedance spectra of plasma electrolytic oxidation coatings on Mg-Zn-Ca alloy in simulated body fluid electrolyte, J. Mater. Sci. 60 (2025) 17232–17253, https://doi.org/10.1007/s10853-025-11339-x.
[31] B. Gault, A. Saksena, X. Sauvage, P. Bagot, L.S. Aota, J. Arlt, L.T. Belkacemi, T. Boll, Y.-S. Chen, L. Daly, M.B. Djukic, J.O. Douglas, M.J. Duarte, P.J. Felfer, R.G. Forbes, J. Fu, H.M. Gardner, R. Gemma, S.S.A. Gerstl, Y. Gong, G. Hachet, S. Jakob, B. M. Jenkins, M.E. Jones, H. Khanchandani, P. Kontis, M. Krämer, M. Kühbach, R.K. W. Marceau, D. Mayweg, K.L. Moore, V. Nallathambi, B.C. Ott, J.D. Poplawsky, T. Prosa, A. Pundt, M. Saha, T.M. Schwarz, Y. Shang, X. Shen, M. Vrellou, Y. Yu, Y. Zhao, H. Zhao, B. Zou, Towards establishing best practice in the analysis of hydrogen and deuterium by atom probe tomography, Microsc. Microanal. (2024), https://doi.org/10.1093/mam/ozae081 ozae081.
[32] A. Devaraj, R. Colby, W.P. Hess, D.E. Perea, S. Thevuthasan, Role of photoexcitation and field ionization in the measurement of accurate oxide stoichiometry by laser-assisted atom probe tomography, J. Phys. Chem. Lett. 4 (2013) 993–998, https://doi.org/10.1021/jz400015h.
[33] S. Pinitsoontorn, A. Cerezo, A.K. Petford-Long, D. Mauri, L. Folks, M.J. Carey, Three-dimensional atom probe investigation of boron distribution in CoFeB/MgO/CoFeB magnetic tunnel junctions, Appl. Phys. Lett. 93 (2008) 071901, https://doi.org/10.1063/1.2973045.
[34] M. Karahka, Y. Xia, H.J. Kreuzer, The mystery of missing species in atom probe tomography of composite materials, Appl. Phys. Lett. 107 (2015) 062105, https://doi.org/10.1063/1.4928625.
[35] F. Vurpillot, A. Bostel, D. Blavette, Trajectory overlaps and local magnification in three-dimensional atom probe, Appl. Phys. Lett. 76 (2000) 3127–3129, https://doi.org/10.1063/1.126545.
[36] X. Wang, C. Hatzoglou, B. Sneed, Z. Fan, W. Guo, K. Jin, D. Chen, H. Bei, Y. Wang, W.J. Weber, Y. Zhang, B. Gault, K.L. More, F. Vurpillot, J.D. Poplawsky, Interpreting nanovoids in atom probe tomography data for accurate local compositional measurements, Nat Commun 11 (2020) 1022, https://doi.org/10.1038/s41467-020-14832-w.
[37] I.E. McCarroll, D. Haley, S. Thomas, M.S. Meier, P.A.J. Bagot, M.P. Moody, N. Birbilis, J.M. Cairney, The effect of hydrogen on the early stages of oxidation of a magnesium alloy, Corros. Sci. 165 (2020) 108391, https://doi.org/10.1016/j.corsci.2019.108391.
[38] T.M. Schwarz, J. Yang, L.S. Aota, E. Woods, X. Zhou, J. Neugebauer, M. Todorova, I. McCarroll, B. Gault, Quasi-"in situ" analysis of the reactive liquid-solid interface during magnesium corrosion using cryo-atom probe tomography, Adv. Mater. 36 (2024) 2401735, https://doi.org/10.1002/adma.202401735.
[39] T.M. Schwarz, N. Birbilis, B. Gault, I. McCarroll, Understanding the Al diffusion pathway during atmospheric corrosion of a Mg-Al alloy using atom probe tomography, Corros. Sci. 252 (2025) 112951, https://doi.org/10.1016/j.corsci.2025.112951.
[40] A. Ghasemi, V.S. Raja, C. Blawert, W. Dietzel, K.U. Kainer, The role of anions in the formation and corrosion resistance of the plasma electrolytic oxidation coatings, Surf. Coat. Technol. 204 (2010) 1469–1478, https://doi.org/10.1016/j.surfcoat.2009.09.069.
[41] G. Rapheal, S. Kumar, N. Scharnagl, C. Blawert, Effect of current density on the microstructure and corrosion properties of plasma electrolytic oxidation (PEO) coatings on AM50 Mg alloy produced in an electrolyte containing clay additives, Surf. Coat. Technol. 289 (2016) 150–164, https://doi.org/10.1016/j.surfcoat.2016.01.033.
[42] P. Bala Srinivasan, J. Liang, C. Blawert, M. Störmer, W. Dietzel, A preliminary study of calcium containing plasma electrolytic oxidation coatings on AM50 magnesium alloy, J. Mater. Sci. 45 (2010) 1406–1410, https://doi.org/10.1007/s10853-009-4093-4.
[43] A. Seyfoori, Sh. Mirdamadi, A. Khavandi, Z.S. Raufi, Biodegradation behavior of micro-arc oxidized AZ31 magnesium alloys formed in two different electrolytes, Appl. Surf. Sci. 261 (2012) 92–100, https://doi.org/10.1016/j.apsusc.2012.07.105.
[44] H. Chen, G. Lv, G. Zhang, H. Pang, X. Wang, H. Lee, S. Yang, Corrosion performance of plasma electrolytic oxidized AZ31 magnesium alloy in silicate solutions with different additives, Surf. Coat. Technol. 205 (2010) S32–S35, https://doi.org/10.1016/j.surfcoat.2010.03.032.
[45] R. Mathieu, G. Libourel, E. Deloule, L. Tissandier, C. Rapin, R. Podor, Na2O solubility in CaO–MgO–SiO2 melts, Geochim. Cosmochim. Acta 75 (2011) 608–628, https://doi.org/10.1016/j.gca.2010.11.001.
[46] X. Lu, S.P. Sah, N. Scharnagl, M. Störmer, M. Starykevich, M. Mohedano, C. Blawert, Mikhail.L. Zheludkevich, K.U. Kainer, Degradation behavior of PEO coating on AM50 magnesium alloy produced from electrolytes with clay particle addition, Surf. Coat. Technol. 269 (2015) 155–169, https://doi.org/10.1016/j.surfcoat.2014.11.027.
[47] X. Lu, C. Blawert, B.J.C. Luthringer, M.L. Zheludkevich, Controllable degradable plasma electrolytic oxidation coated mg alloy for biomedical application, Front. Chem. Eng. 4 (2022), https://doi.org/10.3389/fceng.2022.748549.